Optical Smoothing of Laser Imprinting in Planar-Target Experiments on OMEGA EP Using One-Dimensional Multi-FM Smoothing by Spectral Dispersion

Introduction

One of the primary missions of the National Ignition Facility (NIF)[1] is to experimentally demonstrate ignition with inertial confinement fusion (ICF),[2–4] either by the indirect-drive (or x-ray–drive) approach, where laser beams heat the inside of a high-*Z* enclosure ("hohlraum") in which an implosion capsule is placed,[4] or by the direct-drive approach, where a capsule is illuminated directly by the laser beams to launch the capsule implosion.[5] In ICF the stability of the shell that encases the fusion fuel during the implosion is a key determinant of achieving ignition. Achieving sufficient irradiation uniformity for a successful direct-drive–ignition experiment necessitates the use of single-beam smoothing. Typical requirements for direct-drive illumination are in excess of what is required for indirect-drive illumination since direct drive lacks the inherent smoothing of the radiation field as it flows from the hohlraum wall to the capsule.[6–8]

Shell stability is primarily degraded by the growth of hydrodynamic instabilities that cause both short- and long-wavelength modulations of the shell's areal density. These modulations can result in shell breakup during the acceleration phase of the implosion or lead to a mixing of the cold shell material with the hot fuel,[9] quenching the fusion reactions and reducing target performance during the implosion's deceleration phase. The dominant hydrodynamic instability is the Rayleigh–Taylor (RT) instability.[10,11] It develops during the acceleration phase of the fusion target as the cold dense shell material is accelerated by the hot, low-density blowoff plasma.

In direct-drive targets, initial perturbations that lead to RT growth are primarily seeded by target-surface roughness and nonuniformities of the incident laser intensity ("imprint"). Laser imprinting occurs because spatial variations in the laser intensity drive pressure variations into the target. This distorts the shock and ablation front and creates lateral mass flow in the shock-compressed material, resulting in mass modulations at the ablation surface of the driven target.[12] Various laser-smoothing techniques have been developed to reduce the level of imprinting. These include distributed phase plates (DPP's),[13] continuous-contour phase plates (CPP's),[14] polarization smoothing,[15] induced spatial incoherence (ISI),[16] and smoothing by spectral dispersion (SSD).[17]

SSD varies the interference speckle pattern of a DPP- or CPP-focused laser beam on a shorter time scale than the characteristic hydrodynamic response time of the target, i.e., the imprinting time. This is achieved by adding bandwidth, typically of a few angstroms, to the fundamental laser frequency using an electro-optical modulator. Introducing spectral dispersion to the broadened-bandwidth light, which is focused by including a phase plate, causes the interference structure from beamlets originating at different phase-plate elements to vary in time. At any given moment, the intensity profile is highly modulated because of the interference pattern from the phase-plate–modulated wavefront, but the time-averaged intensity is smoothed.[17]

Some instability mitigation is provided by the SSD system currently installed on the NIF,[18,19] although the level of smoothing is less than that required for direct-drive–ignition experiments.[8] There are two potential paths to implementing SSD beam smoothing for direct-drive ignition on the NIF: (1) Two-dimensional (2-D) SSD, as currently used on the OMEGA laser,[20] has been shown to reduce single-beam irradiation nonuniformities to the few-percent level[21] and to efficiently suppress instability seeds.[22] Adding a comparable 2-D SSD system to the NIF would necessitate major modifications to the preamplifier modules (PAM's) and require additional tripler crystals to convert the extra bandwidth.[8,23] (2) One-dimensional smoothing by spectral dispersion with multiple phase-modulation frequencies (1-D multi-FM SSD)[24,25] was developed at LLE as a more cost-effective and labor-efficient solution to providing the smoothing level required for the current NIF polar-direct-drive–ignition point design. It is compatible with the existing NIF Laser System, and modifications that are necessary to implement 1-D multi-FM SSD on the NIF are limited to fiber-based systems in the Master Oscillator Room, in addition to a new diffraction grating in the PAM.[8] Both 2-D SSD and 1-D multi-FM SSD are predicted to provide the smoothing required by the ignition design.

A prototype multi-FM seed source has been implemented in Beamline 4 of the OMEGA EP laser[26] to validate the predicted multi-FM performance. Amplifying and angularly dispersing the phase-modulated beam in a NIF PAM before injection into Beamline 4 ensures the compatibility of the multi-FM system with the NIF's front end.

The multi-FM performance qualification consists of two parts: (1) measurement of equivalent-target-plane modulations of the laser intensity and (2) validation of the numerical treatment of 1-D multi-FM SSD to predict imprint levels and instability growth with dedicated on-target shots. The remaining sections briefly describe the multi-FM SSD system and its implementation on OMEGA EP; discuss the equivalent-target-plane measurements to characterize modulations in the focal-spot intensity using different SSD methods; describe the experiments that characterize laser-imprint levels by measuring the RT instability growth, including 2-D hydrodynamic simulations of the data; and present our conclusions.

One-Dimensional Multi-FM SSD on OMEGA EP

The implementation of 1-D multi-FM SSD into the front end of Beamline 4 on OMEGA EP is shown schematically in Fig. 147.5. Two separate pulse-shaping systems provide different levels of SSD bandwidth to the laser pulse by transforming the incident electric field $E(t) \propto \exp(i\omega_L t)$ to

$$E(t) \propto \exp\left[i\omega_L t + i\sum_n \delta_n \cos(\omega_n t + \varphi_n)\right]. \quad (1)$$

Here, ω_L is the incident laser frequency; t is the time; and δ_n, ω_n, and φ_n are the modulation depth, frequency, and phase of modulator n, respectively, with the sum being calculated over the number of modulators in the system. The OMEGA EP main-pulse front end introduces bandwidth to the fundamental laser frequency to suppress stimulated Brillouin scattering (SBSS SSD) in the laser system optics. It operates with a modulation frequency of 3 GHz and a modulation depth of 5.5 in the infrared (IR), resulting in a ultraviolet (UV) bandwidth of 0.1 THz. In parallel, a picket-pulse channel provides the bandwidth for the 1-D multi-FM SSD. It comprises three modulators with incommensurate frequencies of 21.2 GHz, 22.8 GHz, and 31.9 GHz and corresponding modulation depths of 0.45, 1.04, and 2.07, respectively. This results in a combined bandwidth in the UV of ~0.5 THz. Multi-FM SSD is typically applied to the early part of the laser pulse during which laser imprint dominates, with SBSS SSD bandwidth applied to the main portion. The two parts are then optically combined to form the desired pulse shape and SSD bandwidth profile. This dynamic bandwidth reduction ensures that the increased bandwidth of multi-FM SSD is not applied during the high-intensity portion of the laser pulse, where it can potentially damage the laser optics.[27] After optical combination, the beam is passed through a diffraction grating, resulting in

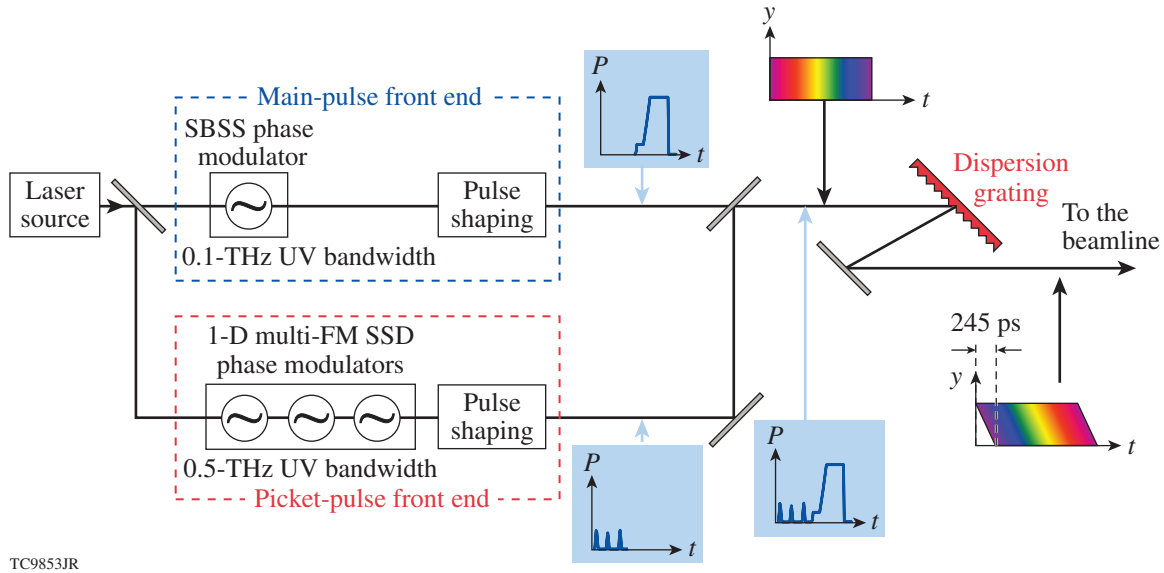

Figure 147.5
One-dimensional multi-FM setup of Beamline 4 on OMEGA EP. Two separate front ends provide bandwidth for either stimulated Brillouin scattering suppression (SBSS) or multi-FM smoothing by spectral dispersion (SSD). The two pulses are then combined optically to form the desired pulse shape and SSD profile. A grating introduces spectral dispersion, resulting in a spatiotemporal shear of 245 ps.

spectral dispersion of the phase-modulated beam and the spatial frequency modulation across the beam necessary for SSD. The grating imposes an uncompensated spatiotemporal shear of Δt = 245 ps to the pulse. Since the NIF laser's front end, for which multi-FM has been designed, is a fiber-based system, it is not possible to place an additional grating in the laser chain before the phase modulators to compensate for this temporal skew. This imposes a minimum rise time of ~250 ps to the portion of the laser pulse to which the multi-FM bandwidth is applied.

For the experiments discussed below, the pulse shapes were generated fully in either the SBSS or the multi-FM SSD front end, without employing dynamic bandwidth reduction.

Equivalent-Target-Plane Measurements

High-resolution, equivalent-target-plane (ETP) measurements of the UV irradiation uniformity of SSD-smoothed laser pulses were performed using the setup shown in Fig. 147.6. The setup is very similar to the UV ETP system on OMEGA, which has been demonstrated to fully resolve individual speckles.[28] After frequency conversion and before focusing into the target chamber, a portion of the Beamline 4 light is picked up using a 4% beam splitter and focused onto a camera with an off-axis parabola. This provides an image of the focal spot equivalent to the on-target conditions with a spatial resolution of ~4 μm. The speckle size w is given by the relationship $w = \lambda f \approx$ 6.5 μm, with λ and f being the laser wavelength and imaging f number, respectively.

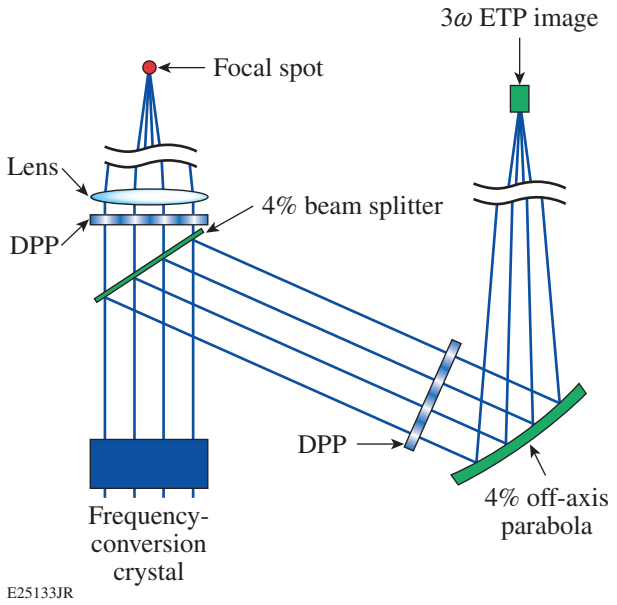

Figure 147.6
The equivalent-target-plane (ETP) diagnostic on OMEGA EP measures the focal-spot profile of a low-power, phase-plate–focused beam with and without SSD bandwidth. DPP: distributed phase plate.

Images of the far-field profile of a wEP-SG8-0800 DPP irradiated with a 2-ns pulse and using different levels of SSD are shown in Fig. 147.7. In addition to the time-integrated far-field data, each image shows central lineouts through the data in the horizontal and vertical directions, below and to the right of the far-field image, respectively. All far-field spots contain the same

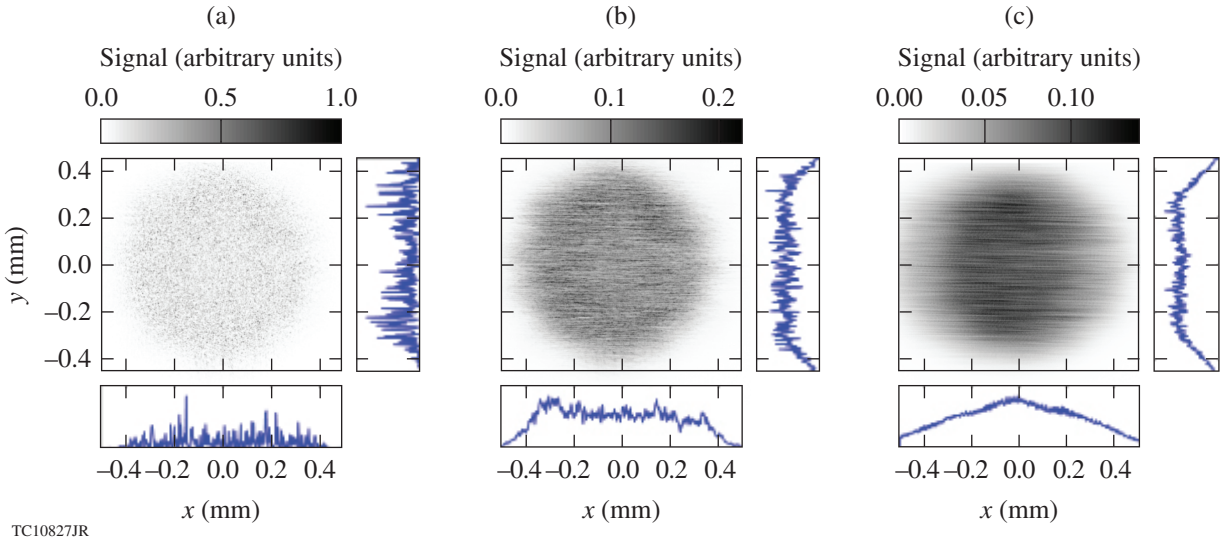

Figure 147.7
Equivalent-target-plane images of the far field of a wEP-SG8-0800 phase plate and central lineouts in the horizontal and vertical directions. (a) With no applied SSD bandwidth, the speckle pattern of the phase-plate–focused far field is well resolved. (b) SBSS SSD and (c) multi-FM SSD applied smoothing in the horizontal direction. The data smoothed by multi-FM SSD are significantly smoother in both the vertical and horizontal directions because of the increased bandwidth.

amount of energy, and the color scales have been adjusted for each image to fully capture the recorded signal range.

The case where no SSD has been applied is shown in Fig. 147.7(a). There is no SSD bandwidth and the speckle pattern is unperturbed and stationary throughout the pulse duration. The speckle pattern is well resolved in the ETP data, and the central lineouts through the data exhibit severe intensity modulations in both the x and y directions. Figure 147.7(b) shows the effect of applying SBSS SSD to the laser pulse. The speckle pattern is displaced in the horizontal direction, smoothing the time-integrated intensity profile. Applying 1-D multi-FM SSD results in the far-field laser spot shown in Fig. 147.7(c)—the smoothest of the three cases shown here—where the intensity modulations in the central lineouts are reduced considerably. Both SBSS SSD and multi-FM SSD apply the angular dispersion in one dimension only, resulting in the smoothing applied predominantly in a single direction (horizontal in Fig. 147.7). As can be seen from the central lineouts, despite the 1-D nature of the applied SSD bandwidth, smoothing is observed in both the x and y directions.

The recorded ETP data agree well with numerical predictions of the smoothing performance. Figure 147.8 shows azimuthally averaged power spectral densities (PSD's) of the far-field data in Fig. 147.7 (blue lines) and the equivalent theoretical predictions (red). The predicted PSD's were calculated by propagating measured near-field phase fronts using the code *Waasikwa*',[29] which incorporates numerical models of the phase plate and SSD. The experimental data agree well with the predictions up to the ETP system resolution at a frequency of ~0.1 μm^{-1}. While SBSS SSD generates a notably smoother profile than in the case of no applied SSD, multi-FM SSD reduces the PSD amplitudes further by ~50% to 70% in the range of 0.01 to 0.1 μm^{-1}, corresponding to modes ~100 to 1000 of an ignition-scale target.

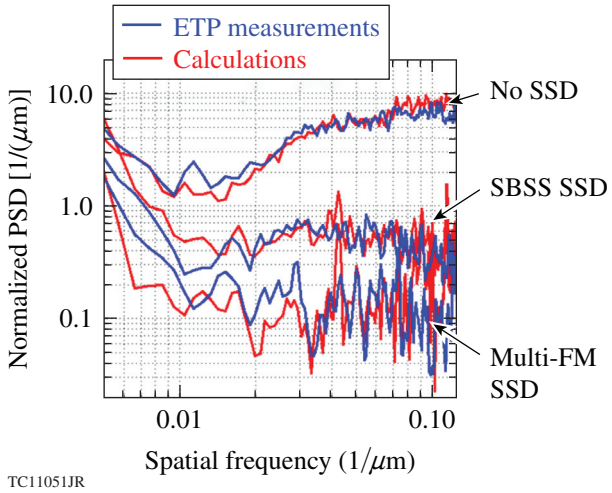

Figure 147.8
The azimuthally averaged power spectral densities of the far-field data in Fig. 147.7 (blue) agree well with the numerical predictions for the different SSD cases (red). Over the plotted frequency range, the power amplitudes are reduced by 50% for multi-FM versus SBSS SSD. PSD: power spectral density.

Measurements and Simulations of Experimental RT Growth

Experiments were performed to study the effect of multi-FM smoothing on laser imprinting in dedicated OMEGA EP target experiments. The experimental setup shown schematically in Fig. 147.9 is based on similar RT-growth experiments per-

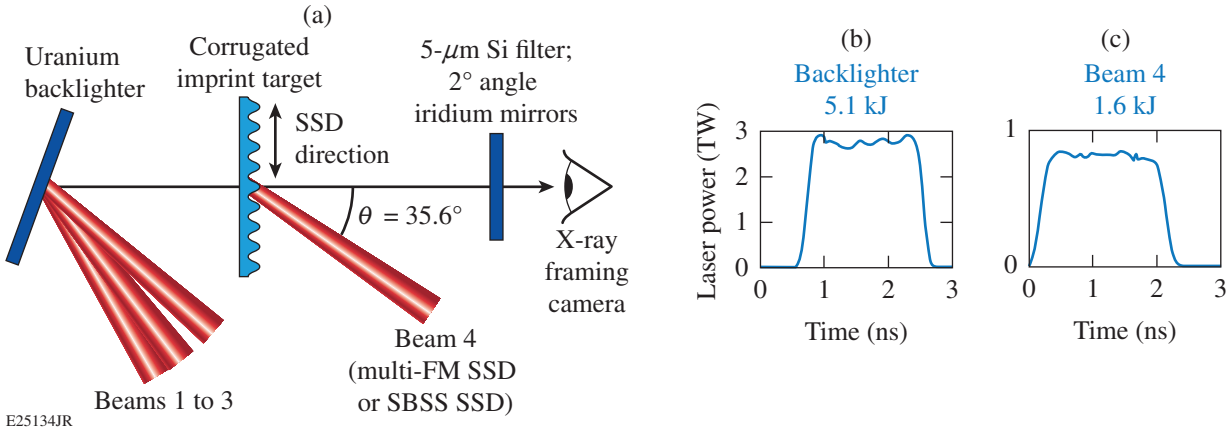

Figure 147.9
Rayleigh–Taylor growth of laser-imprint–seeded modulation and an imposed 30-μm corrugation were tracked by face-on radiography. The spatial variation in the optical depth of the imprint target was recorded using a fast x-ray framing camera giving 100-ps snapshots of the target evolution.

formed on OMEGA.[22,30] A planar, 20-μm-thick CH foil was driven with ~1.6 kJ by Beamline 4 using a 2-ns square pulse with an on-target irradiance of ~10^{14} W/cm^2 and a rise time of ~250 ps, dominated by the temporal skew imposed by the SSD dispersion grating. The imprint target featured a single-mode, sinusoidal surface corrugation with a wavelength of 30 μm and amplitude of 0.1 μm that acts as a reference for the imprint-seeded, broadband RT growth. For a typical ignition-scale direct-drive target, this corresponds to a Legendre mode of ~350 (Ref. 7).

The corrugation was oriented approximately perpendicular to the active SSD direction. The experiments were carried out with either SBSS SSD or multi-FM SSD applied over the full duration of the drive laser. Operation without any SSD bandwidth was not supported because of the potential risk of optics damage in the laser system. The RT-amplified corrugation mode and broadband laser imprint were measured using face-on x-ray radiography of the driven target, providing an optical-depth map of the target at discrete times and highlighting areas of spike and bubble growth. The backlighter was a uranium foil driven with Beamlines 1, 2, and 3 of the OMEGA EP laser with a 2-ns pulse containing a total of ~5 kJ of energy and an on-target irradiance of ~3×10^{14} W/cm^2. An undriven, 3-μm-thick Al foil was placed between the backlighter and the imprint foil. This foil acted as a shield, protecting the imprint target from plasma blowoff generated at the backlighter, as well as from soft x-ray emission that could preheat the imprint target. X rays transmitted through the Al heat shield and the imprint target were imaged with 10-μm pinholes onto a fast x-ray framing camera.[31] A combination of iridium-coated, grazing-incidence mirrors oriented at a 2° angle of incidence and 5-μm-thick Si filtering limited the recorded x-ray energy to ~1.5 keV. The x-ray framing camera recorded multiple snapshots of the target's optical depth over an ~1-ns window, with individual images integrated over the camera gate width of ~100 ps. This radiography technique lacks the sensitivity to measure imprint levels or the preimposed corrugation feature directly and relies on RT growth of the target modulations to produce detectable levels of variation in optical depth.

Unlike previous planar-target imprint experiments performed on OMEGA (see, e.g., Ref. 22), in the experiments discussed here the imprint target was irradiated from the side facing the detector (compare Fig. 147.9). Driving the imprint target from the rear is the preferred option since the CH target itself acts as a filter for its own self-emission. The reverse geometry for the multi-FM measurements, however, is necessitated by the beam and diagnostics layout on OMEGA EP, where all beams originate from the same direction. At an x-ray energy of 1.5 keV, the energy used to probe the optical-depth evolution, a 20-μm-thick plastic foil attenuates the x-ray flux to ~25%. This drops the achievable signal-to-noise ratio in these experiments by approximately a factor of 4 compared to a rear-driven geometry since the backlighter emission competes with higher levels of self-emission.

To extract the evolution of modulation amplitudes, the optical-depth maps are converted into frequency space by Fourier transformation. Examples of experimental optical-depth maps are shown in Fig. 147.10, with Fig. 147.10(a) using SBSS SSD and Fig. 147.10(b) using 1-D multi-FM SSD; Figs. 147.10(c) and 147.10(d) are the equivalent frequency maps, respectively. The optical-depth maps, plotted on the same color scale, were obtained ~1.75 ns after the onset of the laser drive. In these data, the initially imposed corrugation is oriented vertically; i.e., lines of equal amplitude are parallel to the y direction, and the active SSD direction is approximately horizontal. While the corrugation mode is more dominant in the multi-FM–smoothed data, the corrugation is well resolved in both data sets, appear-

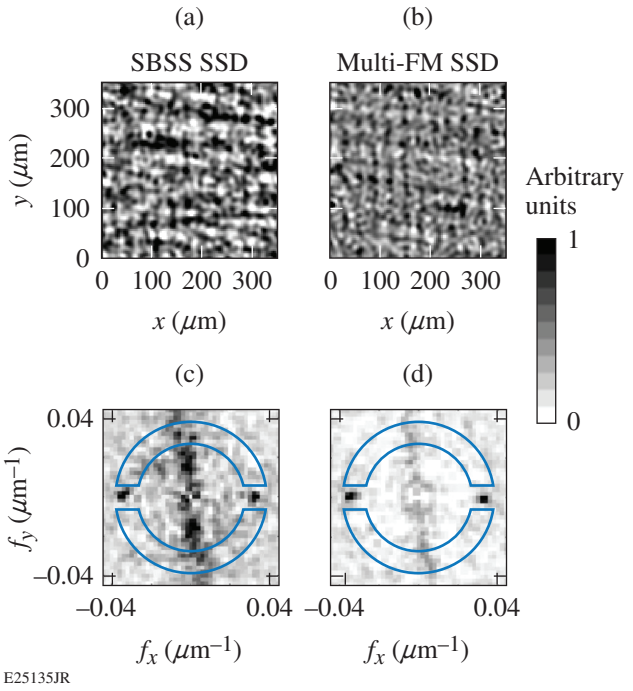

Figure 147.10
[(a),(b)] Optical-depth data with SBSS SSD and multi-FM SSD, respectively. The 30-μm corrugation appears as vertical lines, with SSD acting mainly in the horizontal direction. In frequency space [(c),(d)] the corrugation appears as a single peak at f_x = 1/30 μm^{-1}. Because of the 1-D nature of multi-FM SSD, broadband imprint is predominantly located along f_y for $f_x \sim 0$. The semicircles denote the analysis region for the $f \sim$ 1/30-μm broadband mode.

ing as vertical lines in the optical depth, and as a single peak in frequency space for $f_x = 1/30\ \mu\text{m}^{-1}$ and $f_y = 0$. In both cases, broadband imprint and RT growth are predominantly visible in the direction perpendicular to the active SSD smoothing, appearing as irregular structures in the horizontal direction in the optical-depth data and elevated mode amplitudes in the f_y direction for $f_x \sim 0$ in the frequency maps. The data are oriented such that the corrugation feature falls at $f_y = 0$, while a slight target misalignment resulted in the direction of least smoothing (i.e., perpendicular to the active SSD direction) at $\varphi \approx 98°$. The broadband-imprint feature along this direction is noticeably broader in f_x for the SBSS data [Fig. 147.10(c)] than in the multi-FM case [Fig. 147.10(d)], as expected from the improved smoothing of 1-D multi-FM SSD.

To calculate areal density from the measured optical depth, the backlighter emission was characterized by radiographing an undriven sample target in a dedicated experiment. The sample target was made of the same CH material as the imprint target and comprised multiple steps of known CH thickness. This calibration experiment directly relates experimental optical depth and target areal densities and confirms a central backlighter energy of ~1.5 keV.

The experimentally measured evolution of the 30-μm corrugation is shown in Fig. 147.11(a), plotting the areal-density amplitude as a function of time. The circles denote data recorded with 1-D multi-FM SSD applied to the drive laser, while the squares denote data taken with SBSS SSD. Since the corrugation mode is preimposed and not an imprint feature, its growth and absolute amplitude should be independent of the applied SSD bandwidth, as confirmed by the experimental data. The data points in Fig. 147.11(b) show the root-mean-square (rms) amplitude of the broadband 30-μm imprint, corresponding to the azimuthally integrated $f \sim 1/30\text{-}\mu\text{m}^{-1}$ mode in frequency space, but excluding a region of $\Delta f_x = \Delta f_y = 1/250^{-1}\ \mu$m centered around the corrugation peak at $f_x = 1/30\ \mu\text{m}^{-1}$ and $f_y = 0$. The integration range is marked by the region inside the two semicircles overlaid onto the frequency space maps in Figs. 147.10(c) and 147.10(d). These data were recorded on the same shots as the data shown in Fig. 147.11(a). While there is considerable noise in the data, the SBSS-smoothed amplitudes consistently exceed the multi-FM case by a factor of ~2.

Simulation results for the growth of the corrugation mode and the rms amplitude of the $f \sim 1/30\text{-}\mu$m broadband imprint mode are shown as the solid lines in Figs. 147.11(a) and 147.11(b), respectively. The target evolution was simulated using the 2-D radiation–hydrodynamics code *DRACO*,[32] which

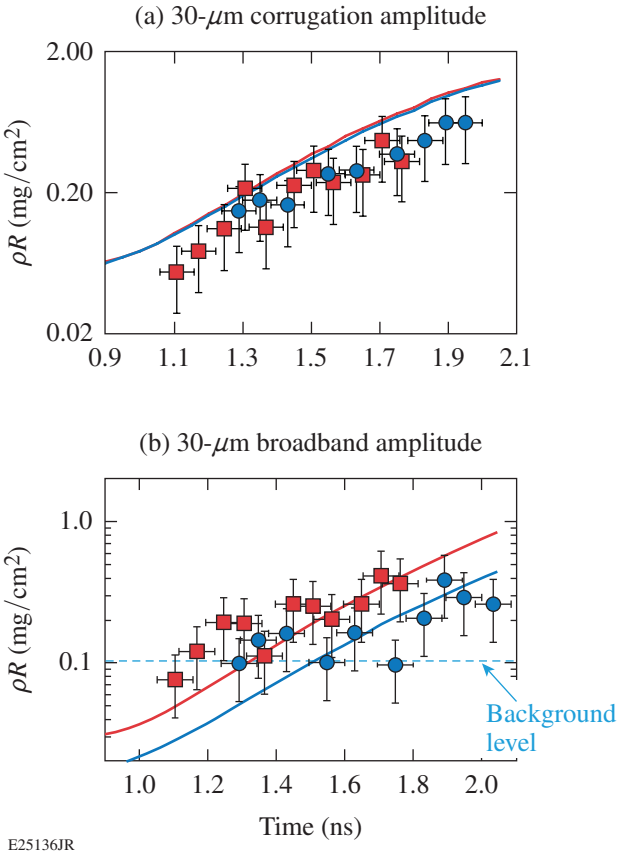

Figure 147.11
(a) Time evolution of the 30-μm experimental (data points) and simulated (lines) corrugation amplitudes. The red squares denote data acquired with SBSS SSD and the blue circles denote data acquired with multi-FM SSD. The corrugated mode is not affected by imprint and exhibits a growth rate independent of the SSD bandwidth. (b) Root-mean-square (rms) amplitude of the experimental (data points) and simulated (lines) broadband 30-μm mode. The dashed horizontal line denotes the background level in the experimental data. The red and blue lines are 2-D *DRACO* simulated growth rates for SBSS and multi-FM, respectively.

includes a 3-D ray-trace package to model the laser absorption. The effect of the SSD bandwidth is taken into account by calculating the far-field laser spots multiple times per picosecond using the code *Waasikwa*'.[29] The code uses the near-field laser intensity and phase, including the SSD bandwidth and its effect, and propagates it through the phase plate and the main lens to obtain an instantaneous far field. Figure 147.12(a) illustrates a laser beam's near-field lineout along the SSD active direction as a function of time, with different colors illustrating the change in light frequency related to the SSD bandwidth. The temporal skew caused by the uncompensated diffraction grating in the SSD chain results in an initially sub-aperture beam incident onto the DPP, which gradually increases in area to full aperture by the end of the 245-ps skew interval. The action of 1-D SSD and an uncompensated diffraction grating result in an asym-

metric and time-dependent far-field spot and speckle pattern, as illustrated in Figs. 147.12(b) and 147.12(c), which show calculated far-field profiles at 20 ps and 100 ps, respectively.

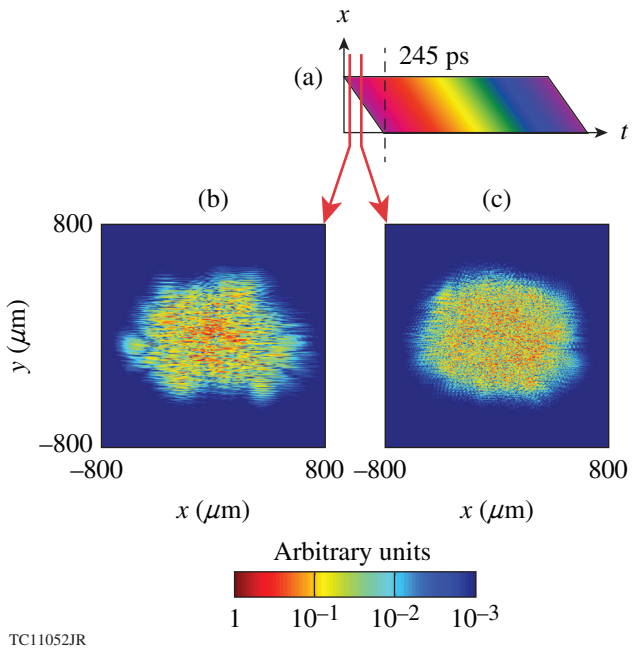

Figure 147.12
(a) Illustration of the laser beam's near field along the SSD active direction versus time. [(b),(c)] Far fields calculated by *Waasikwa*' from instantaneous near fields at times of 20 ps and 100 ps, respectively.

To fully simulate the interaction of the 1-D multi-FM and SBSS SSD-smoothed laser beams with the target requires a 3-D hydrocode and a 3-D ray trace. In such calculations, the instantaneous far fields would be used to assign the energy of rays launched at the outer boundary of the simulation region, which would then be traced through the plasma, depositing their energy in cells of the simulation mesh by the inverse bremsstrahlung process, capturing the asymmetry of the SSD action with respect to the target's x and y coordinates. In 2-D cylindrical hydro simulations with a 3-D ray trace, however, such as used for the simulations presented here, the x and y coordinates are reduced to a single axis by averaging the laser deposition along the azimuthal angle φ. This makes it impossible to capture the effect of SSD with a single 2-D calculation. It is possible to simplify the problem, however, by taking advantage of the fact that at early stages of the laser drive, the nonuniformities are small and the RT growth is in its linear stage. During the linear stage, individual modulation modes do not interact with each other and can be considered independently. This allows one to reproduce the 3-D nature of the experiment with a set of 2-D hydrocode simulations in which each simulation considers only a single frequency slice of the incident far-field spectrum.

As illustrated in Fig. 147.13, the full 3-D target response was calculated by dividing the instantaneous, incident far field [Fig. 147.13(a)] into 120 frequency slices at a 3° separation

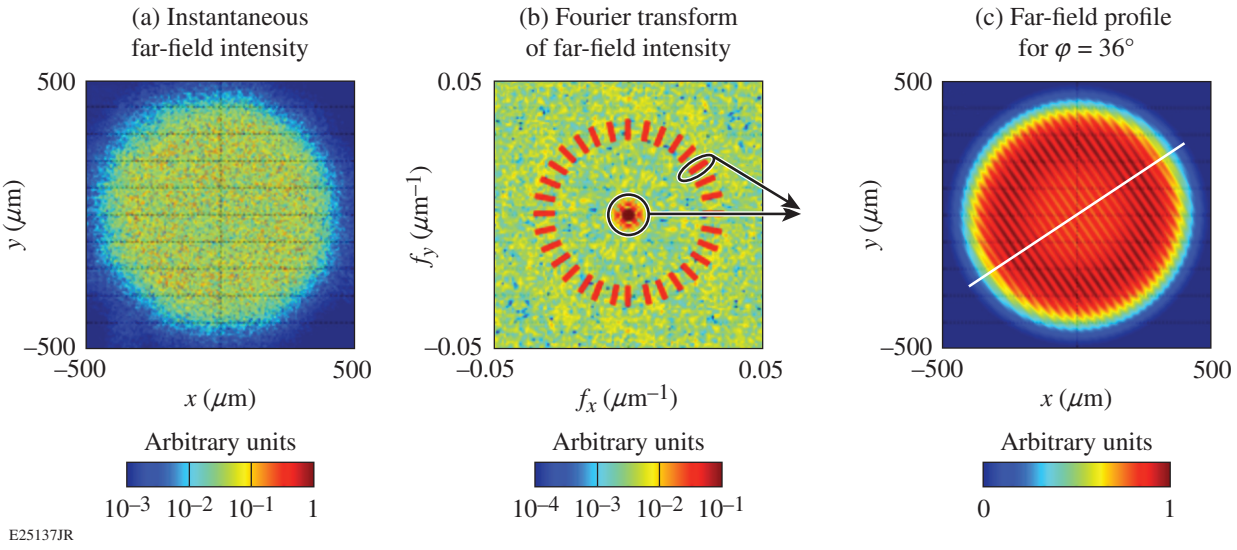

Figure 147.13
Combining multiple 2-D simulations using a reduced far-field spot as the input captured the 3-D experimental imprint. The instantaneous laser far field (a) is converted into frequency space (b) and divided into 120 frequency slices with 3° separation. (c) The reduced far-field spot for $\varphi = 36°$ is constructed by combining the low-spatial-frequency envelope with the 29- to 31-μm wavelength range of the $\varphi = 36°$ frequency slice.

[Fig. 147.13(b)]. Combining the time-varying, low-spatial-frequency envelope at the center of the frequency map with the Fourier modes with the 29- to 31-μm wavelengths contained within each frequency slice gives a "reduced" far-field spot. This reduced far-field spot contains modulations in only a single direction, as determined by the selected frequency slice, and can be used as an input for a 2-D simulation. An example of such a reduced far field [Fig. 147.13(c)] shows the far-field spot for the $\varphi = 36°$ frequency slice. In these 2-D calculations, the initial target corrugation was included in only the frequency slice for $\varphi = 0°$; i.e., along the 1-D multi-FM SSD active direction and the direction of the most-efficient smoothing.

Individual frequency-slice calculations that emulate the effect of 1-D multi-FM SSD are presented in Fig. 147.14. These images show mass-density profiles of the accelerated foil at 1.75 ns. Figure 147.14(a) shows the case for the frequency slice at $\varphi = 90°$ (along the vertical axis and perpendicular to the multi-FM SSD active direction); Fig. 147.14(b) shows the case for the frequency slice at $\varphi = 69°$. The smoothing is least efficient perpendicular to the SSD active direction, and the density profile shown in Fig. 147.14(a) has noticeable RT growth, resulting from far-field–spot modulations and laser imprint. In contrast, the profile in Fig. 147.14(b) exhibits very little growth, emphasizing how 1-D multi-FM SSD efficiently suppresses imprint modes that have a non-negligible component along the active SSD direction.

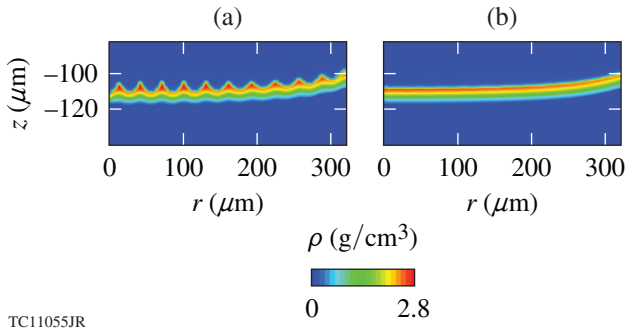

Figure 147.14
Profiles of the calculated foil density at 1.75 ns using 1-D multi-FM SSD for two of the 120 laser far-field frequency slices with wavelengths of 29 to 30 μm. (a) The least amount of imprint mitigation is found for the far-field frequency component perpendicular to the active SSD direction. (b) At 69° off the active SSD direction, imprint is already significantly reduced.

As shown in Fig. 147.15, *DRACO* simulations reproduce imprint and corrugation features seen in the Fourier space of the experimental optical-depth maps, such as the directionality of the SSD observed in frequency space (compare to Fig. 147.10). The broadband imprint is dominated by Fourier modes perpendicular to the active SSD direction and close to $f_x \sim 0$, while the modes with $f_x \neq 0$ are effectively removed by the SSD (more so in the case of multi-FM than SBSS SSD).

The simulated corrugation amplitudes versus time are shown in Fig. 147.11(a) as the solid lines. While the growth rate observed in the experiment is reproduced correctly, the simulation exhibits a 40%-higher amplitude compared to the experimental data. The source of the disagreement between the experimental growth of the preimposed corrugation and its simulation is currently unknown, but it is likely caused by a combination of the background in the data or an uncharacterized level of surface roughness of the imprint foil. The simulated broadband imprint amplitudes of the nonuniformities at a frequency of 1/30 μm^{-1} are shown in Fig. 147.11(b) for the SBSS (red line) and multi-FM SSD case (blue line). The numerical calculations reproduce the experimental data within the error bars once the data exceed the background level. The simulations predict an ~2× reduction of the imprint level for the multi-FM SSD case compared to the SBSS SSD case, consistent with the experimental data. The calculations further reproduce

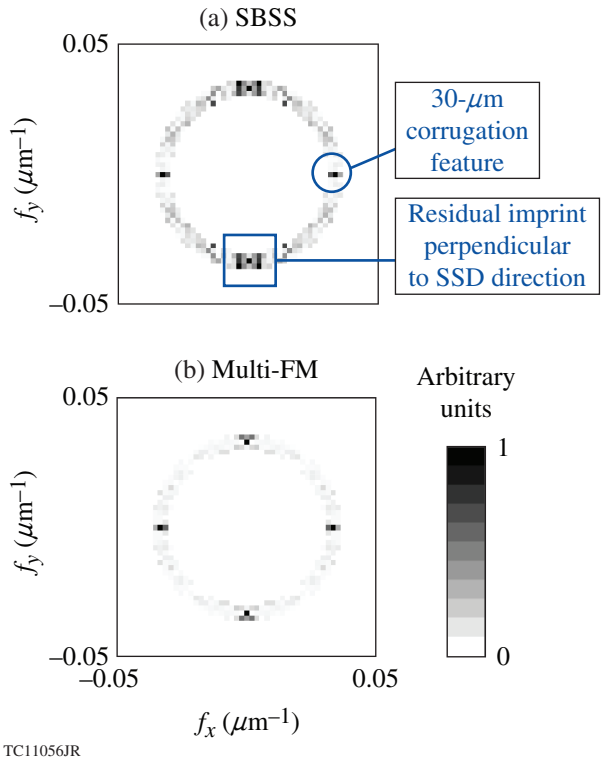

Figure 147.15
Fourier transform of *DRACO*-simulated optical depth at 1.75 ns for $f \sim 1/30$ μm using (a) SBSS SSD and (b) multi-FM SSD.

the directionality of SSD observed in frequency space [compare Fig. 147.15 and Figs. 147.10(c) and 147.10(d)]. The broadband imprint is dominated by Fourier modes perpendicular to the active SSD direction and close to $f_x \sim 0$, while the modes with $f_x \neq 0$ are effectively removed by SSD (more so in the case of multi-FM than SBSS SSD).

Conclusions

In summary, 1-D multi-FM SSD beam smoothing was developed at LLE to provide sufficient far-field uniformity for direct-drive inertial confinement fusion applications at the National Ignition Facility. A prototype of the multi-FM system has been implemented in the NIF-like Beamline 4 on the OMEGA EP laser for verification purposes. Multi-FM SSD beam-smoothing performance was verified with both equivalent-target-plane measurements of the laser's far field and in dedicated planar-target experiments by comparing smoothing rates with SBSS SSD and multi-FM SSD. Numerical calculations using the code *Waasikwa*' agree well with measurements of the multi-FM–smoothed, far-field spatial frequency spectrum. In the planar-target experiments, Rayleigh–Taylor growth rates of laser-imprinted and preimposed surface modulations at $f \sim$ 1/30 μm were measured by face-on x-ray radiography. As expected, the growth of the preimposed surface corrugation is independent of the SSD bandwidth, while 1-D multi-FM SSD is observed to reduce imprint levels by ~50% compared to SBSS SSD. The target experiment was simulated using the 2-D hydrodynamics code *DRACO* and realistic, time-dependent, far-field spot intensity calculations that included the effect of SSD. The 3-D nature of the imprint experiment was captured in the 2-D calculations by 120 individual simulations of a reduced far-field spot, containing only broadband modes in a single 2-D frequency slice. Within the error bars, the simulations correctly reproduce the relative and absolute amplitude levels between multi-FM and SBSS-SSD–smoothed broadband data, but they fail to capture the absolute amplitudes of the preimposed corrugation mode. An experimental unknown, such as surface roughness or an unaccounted-for background level, may be the cause of this discrepancy. Despite this discrepancy, the experimental data show a clear enhancement in smoothing performance of multi-FM SSD compared to SBS-suppression SSD, in agreement with simulations.

ACKNOWLEDGMENT

This material is based upon work supported by the Department of Energy National Nuclear Security Administration under Award Number DE-NA0001944, the University of Rochester, and the New York State Energy Research and Development Authority. The support of DOE does not constitute an endorsement by DOE of the views expressed in this article.

REFERENCES

1. G. H. Miller, E. I. Moses, and C. R. Wuest, Opt. Eng. **43**, 2841 (2004).
2. J. Nuckolls *et al*., Nature **239**, 139 (1972).
3. J. D. Lindl, *Inertial Confinement Fusion: The Quest for Ignition and Energy Gain Using Indirect Drive* (Springer-Verlag, New York, 1998).
4. S. Atzeni and J. Meyer-ter-Vehn, *The Physics of Inertial Fusion: Beam Plasma Interaction, Hydrodynamics, Hot Dense Matter, International Series of Monographs on Physics* (Clarendon Press, Oxford, 2004).
5. R. S. Craxton, K. S. Anderson, T. R. Boehly, V. N. Goncharov, D. R. Harding, J. P. Knauer, R. L. McCrory, P. W. McKenty, D. D. Meyerhofer, J. F. Myatt, A. J. Schmitt, J. D. Sethian, R. W. Short, S. Skupsky, W. Theobald, W. L. Kruer, K. Tanaka, R. Betti, T. J. B. Collins, J. A. Delettrez, S. X. Hu, J. A. Marozas, A. V. Maximov, D. T. Michel, P. B. Radha, S. P. Regan, T. C. Sangster, W. Seka, A. A. Solodov, J. M. Soures, C. Stoeckl, and J. D. Zuegel, Phys. Plasmas **22**, 110501 (2015).
6. P. W. McKenty, V. N. Goncharov, R. P. J. Town, S. Skupsky, R. Betti, and R. L. McCrory, Phys. Plasmas **8**, 2315 (2001).
7. T. J. B. Collins, J. A. Marozas, K. S. Anderson, R. Betti, R. S. Craxton, J. A. Delettrez, V. N. Goncharov, D. R. Harding, F. J. Marshall, R. L. McCrory, D. D. Meyerhofer, P. W. McKenty, P. B. Radha, A. Shvydky, S. Skupsky, and J. D. Zuegel, Phys. Plasmas **19**, 056308 (2012).
8. M. Hohenberger, P. B. Radha, J. F. Myatt, S. LePape, J. A. Marozas, F. J. Marshall, D. T. Michel, S. P. Regan, W. Seka, A. Shvydky, T. C. Sangster, J. W. Bates, R. Betti, T. R. Boehly, M. J. Bonino, D. T. Casey, T. J. B. Collins, R. S. Craxton, J. A. Delettrez, D. H. Edgell, R. Epstein, G. Fiksel, P. Fitzsimmons, J. A. Frenje, D. H. Froula, V. N. Goncharov, D. R. Harding, D. H. Kalantar, M. Karasik, T. J. Kessler, J. D. Kilkenny, J. P. Knauer, C. Kurz, M. Lafon, K. N. LaFortune, B. J. MacGowan, A. J. Mackinnon, A. G. MacPhee, R. L. McCrory, P. W. McKenty, J. F. Meeker, D. D. Meyerhofer, S. R. Nagel, A. Nikroo, S. Obenschain, R. D. Petrasso, J. E. Ralph, H. G. Rinderknecht, M. J. Rosenberg, A. J. Schmitt, R. J. Wallace, J. Weaver, C. Widmayer, S. Skupsky, A. A. Solodov, C. Stoeckl, B. Yaakobi, and J. D. Zuegel, Phys. Plasmas **22**, 056308 (2015).
9. D. K. Bradley, J. A. Delettrez, R. Epstein, R. P. J. Town, C. P. Verdon, B. Yaakobi, S. Regan, F. J. Marshall, T. R. Boehly, J. P. Knauer, D. D. Meyerhofer, V. A. Smalyuk, W. Seka, D. A. Haynes, Jr., M. Gunderson, G. Junkel, C. F. Hooper, Jr., P. M. Bell, T. J. Ognibene, and R. A. Lerche, Phys. Plasmas **5**, 1870 (1998).
10. S. E. Bodner, Phys. Rev. Lett. **33**, 761 (1974).
11. S. Chandrasekhar, in *Hydrodynamic and Hydromagnetic Stability, International Series of Monographs on Physics* (Clarendon Press, Oxford, 1961).
12. V. N. Goncharov, S. Skupsky, T. R. Boehly, J. P. Knauer, P. McKenty, V. A. Smalyuk, R. P. J. Town, O. V. Gotchev, R. Betti, and D. D. Meyerhofer, Phys. Plasmas **7**, 2062 (2000).
13. Y. Lin, T. J. Kessler, and G. N. Lawrence, Opt. Lett. **21**, 1703 (1996).
14. S. N. Dixit *et al*., Proc. SPIE **2633**, 141 (1995).

15. T. R. Boehly, V. A. Smalyuk, D. D. Meyerhofer, J. P. Knauer, D. K. Bradley, R. S. Craxton, M. J. Guardalben, S. Skupsky, and T. J. Kessler, J. Appl. Phys. **85**, 3444 (1999).

16. R. H. Lehmberg and S. P. Obenschain, Opt. Commun. **46**, 27 (1983).

17. S. Skupsky, R. W. Short, T. Kessler, R. S. Craxton, S. Letzring, and J. M. Soures, J. Appl. Phys. **66**, 3456 (1989).

18. B. J. MacGowan *et al*., Phys. Plasmas **3**, 2029 (1996).

19. C. A. Haynam *et al*., Appl. Opt. **46**, 3276 (2007).

20. T. R. Boehly, D. L. Brown, R. S. Craxton, R. L. Keck, J. P. Knauer, J. H. Kelly, T. J. Kessler, S. A. Kumpan, S. J. Loucks, S. A. Letzring, F. J. Marshall, R. L. McCrory, S. F. B. Morse, W. Seka, J. M. Soures, and C. P. Verdon, Opt. Commun. **133**, 495 (1997).

21. S. P. Regan, J. A. Marozas, R. S. Craxton, J. H. Kelly, W. R. Donaldson, P. A. Jaanimagi, D. Jacobs-Perkins, R. L. Keck, T. J. Kessler, D. D. Meyerhofer, T. C. Sangster, W. Seka, V. A. Smalyuk, S. Skupsky, and J. D. Zuegel, J. Opt. Soc. Am. B **22**, 998 (2005).

22. T. R. Boehly, V. N. Goncharov, O. Gotchev, J. P. Knauer, D. D. Meyerhofer, D. Oron, S. P. Regan, Y. Srebro, W. Seka, D. Shvarts, S. Skupsky, and V. A. Smalyuk, Phys. Plasmas **8**, 2331 (2001).

23. S. Skupsky and R. S. Craxton, Phys. Plasmas **6**, 2157 (1999).

24. *LLE Review Quarterly Report* **114**, 73, Laboratory for Laser Energetics, University of Rochester, Rochester, NY, LLE Document No. DOE/NA/28302-826, NTIS Order No. DE2008935224 (2008).

25. J. A. Marozas, J. D. Zuegel, and T. J. B. Collins, Bull. Am. Phys. Soc. **55**, 294 (2010).

26. L. J. Waxer, M. J. Guardalben, J. H. Kelly, B. E. Kruschwitz, J. Qiao, I. A. Begishev, J. Bromage, C. Dorrer, J. L. Edwards, L. Folnsbee, S. D. Jacobs, R. Jungquist, T. J. Kessler, R. W. Kidder, S. J. Loucks, J. R. Marciante, D. N. Maywar, R. L. McCrory, D. D. Meyerhofer, S. F. B. Morse, A. V. Okishev, J. B. Oliver, G. Pien, J. Puth, and A. L. Rigatti, in *Conference on Lasers and Electro-Optics/Quantum Electronics and Laser Science Conference and Photonic Applications Systems Technologies, OSA Technical Digest* (CD) (Optical Society of America, Washington, DC, 2008), Paper JThB1.

27. *LLE Review Quarterly Report* **85**, 39, Laboratory for Laser Energetics, University of Rochester, Rochester, NY, LLE Document No. DOE/SF/19460-378, PB2006106656 (2000).

28. S. P. Regan, J. A. Marozas, J. H. Kelly, T. R. Boehly, W. R. Donaldson, P. A. Jaanimagi, R. L. Keck, T. J. Kessler, D. D. Meyerhofer, W. Seka, S. Skupsky, and V. A. Smalyuk, J. Opt. Soc. Am. B **17**, 1483 (2000).

29. J. A. Marozas, S. P. Regan, J. H. Kelly, D. D. Meyerhofer, W. Seka, and S. Skupsky, J. Opt. Soc. Am. B **19**, 7 (2002).

30. V. A. Smalyuk, T. R. Boehly, D. K. Bradley, V. N. Goncharov, J. A. Delettrez, J. P. Knauer, D. D. Meyerhofer, D. Oron, D. Shvarts, Y. Srebro, and R. P. J. Town, Phys. Plasmas **6**, 4022 (1999).

31. D. K. Bradley *et al*., Rev. Sci. Instrum. **66**, 716 (1995).

32. P. B. Radha, V. N. Goncharov, T. J. B. Collins, J. A. Delettrez, Y. Elbaz, V. Yu. Glebov, R. L. Keck, D. E. Keller, J. P. Knauer, J. A. Marozas, F. J. Marshall, P. W. McKenty, D. D. Meyerhofer, S. P. Regan, T. C. Sangster, D. Shvarts, S. Skupsky, Y. Srebro, R. P. J. Town, and C. Stoeckl, Phys. Plasmas **12**, 032702 (2005).